Title: **Gas Hydrate Dissociation in Sediments: Pressure-Temperature Evolution**

Authors: Tae-Hyuk Kwon
Graduate Student, Department of Civil and Environmental Engineering,
Korea Advanced Institute of Science and Technology (KAIST), Daejeon 305-701, Korea
Tel: +82-42-869-5662
Fax: +82-42-869-3610
Email: kikig@kaist.ac.kr

Gye-Chun Cho
Associate Professor, Department of Civil and Environmental Engineering,
Korea Advanced Institute of Science and Technology (KAIST), Daejeon 305-701, Korea
Tel: +82-42-869-3622
Fax: +82-42-869-3610
Email: gyechun@kaist.edu

J. Carlos Santamarina
Professor, School of Civil and Environmental Engineering,
Georgia Institute of Technology,
790 Atlantic Dr. Atlanta, GA 30332, USA
Tel: +1-404-894-7605
Fax: +1-404-894-2281
Email: jcs@gatech.edu

Corresponding Author: Gye-Chun Cho

Number of word: 3418 (without references, figures or tables)

Number of table: 4

Number of figure: 8

Keyword: Pressure Evolution, Excess Pore Pressure, Gas Hydrate, Dissociation, Self preservation, Hydrate-bearing Sediments

Abstract

Hydrate-bearing sediments may destabilize spontaneously as part of geological processes, unavoidably during petroleum drilling/production operations, or intentionally as part of gas extraction from the hydrate itself. In all cases, high pore fluid pressure generation is anticipated during hydrate dissociation. A comprehensive formulation is derived for the prediction of fluid pressure evolution in hydrate-bearing sediments subjected to thermal stimulation without mass transfer. The formulation considers pressure and temperature-dependent volume changes in all phases, effective stress-controlled sediment compressibility, capillarity, and the relative solubilities of fluids. Salient implications are explored through parametric studies. The model properly reproduces experimental data, including the PT evolution along the phase boundary during dissociation, and the effect of capillarity. Pore fluid pressure generation is proportional to the initial hydrate fraction and the sediment bulk stiffness; is inversely proportional to the initial gas fraction and gas solubility and is limited by changes in effective stress that cause the failure of the sediment. When the sediment stiffness is high, the generated pore pressure reflects thermal and pressure changes in water, hydrate, and mineral densities. Comparative analyses for CO_2 and CH_4 highlight the role of gas solubility in excess pore fluid pressure generation. Dissociation in small pores experiences melting point depression due to changes in water activity, and lower pore fluid pressure generation due to the higher gas pressure in small gas bubbles. Capillarity effects may be disregarded in silts and sands, when hydrates are present in nodules and lenses, and when the sediment experiences hydraulic fracture.

1. Introduction

Hydrate-bearing sediments are found in continental margins and permafrost where pressure and temperature satisfy stability conditions. At the pore scale, hydrates exist in disseminated form in coarse-grained sediments, or are concentrated in nodules and lenses in fine-grained silty or clayey deposits [*Dillon and Max*, 2000].

Hydrate-bearing sediments may destabilize spontaneously as part of geological processes, unavoidably during petroleum drilling/production operations [*Briaud and Chaouch*, 1997], or intentionally as part of gas extraction from the hydrate itself. Potential gas production methods include depressurization, inhibitor injection, thermal stimulation, and their combinations [*Holder et al.*, 1984; *Moridis*, 2003; *Pawar et al.*, 2005].

High pore fluid pressure generation is anticipated during hydrate dissociation. One unit volume of methane hydrate V_0 dissociates at a constant pressure of 10 MPa to occupy a combined volume of $2.62V_0$ (where water and gas volumes are $V_W = 0.79V_0$ and $V_G = 1.83V_0$). Assuming the final pressure and temperature to be 1 atm and 20°C, the final combined volume would be $183.95V_0$ ($V_W = 0.79V_0$ and $V_G = 183.16V_0$). Such a large volume expansion would cause the development of high fluid pressure and/or large fluid flux. Furthermore, the effective stress-dependent sediment stiffness, shear strength and fluid conduction would be affected by changes in the pore fluid pressure [*Briaud and Chaouch*, 1997; *Birchood et al.*, 2005; *Nixon and Grozic*, 2007].

Clearly, pressure generation depends on the initial volume fraction of the phases (including

gas, e.g., at the base of the gas hydrate stability zone), the rates of fluid flow, heat flux and pressure generation, and the global volume change experienced by the hydrate-bearing sediment [*Ullerich et al.*, 1987; *Kayen and Lee*, 1991; *Sultan et al.*, 2004; *Xu and Germanovich*, 2006].

Reliable predictions of gas production, pressure evolution and fluid flow are required in relation to any possible dissociation event. The purpose of this study is to derive a comprehensive formulation to predict the evolution of fluid pressure as a result of hydrate dissociation in sediments subjected to thermal stimulation. The formulation is extended to take into consideration sediment compressibility and capillary effects. It is then applied in a comparative analysis of methane and carbon dioxide hydrate bearing sediments, and is validated with experimental data. The manuscript starts with a discussion of concurrent events taking place during hydrate dissociation in sediments.

2. Underlying Processes

Consider a mass of gas hydrate within the stability zone, away from the phase transformation boundary, subjected to a gradual increase in temperature. The following processes develop as temperature increases (refer to Figure 1).

Gas solubility. In the absence of hydrates, gas solubility in water increases as temperature decreases and pressure increases, as prescribed in Henry's law [*Lide*, 1997; *Osegovic et al.*, 2006]. The presence of hydrates facilitates further hydrate formation, and hence the

equilibrium concentration of gas in water decreases and gas solubility in water increases with temperature [*Handa*, 1990; *Aya et al.*, 1997; *Davie et al.*, 2004; *Servio and Englezos*, 2001; *Duan and Mao*, 2006]; this observation applies to the A-B path in the stability "$H+L_w$" zone in Figure 1. Eventually, gas solubilities in water with and without hydrate converge at the phase boundary P-T. Accordingly, Henry's law applies along the B-C-D path in Figure 1.

Dissolution. The increase in temperature within the stability zone (A-to-B in Figure 1) causes an initial breakdown of the hydrate structure due to the increased gas solubility in the surrounding pore water. "Hydrate dissolution" generates water and dissolved gas; there is no free gas produced. A significant, yet relatively small pore pressure change accompanies dissolution [*Sultan et al.*, 2004; *Sultan*, 2007; *Xu and Germanovich*, 2007].

Dissociation. Hydrate dissociation starts when the PT state reaches the equilibrium boundary (point B in Figure 1). During isochoric heating, the PT state remains on the phase boundary until all hydrate dissociates (B-to-C in Figure 1); this response has been conveniently used to identify the phase boundary [*Marshall et al.*, 1964; *Schroeter et al.*, 1983]. Dissociation produces free gas, gas-saturated water, and water vapor saturated gas. The pronounced volume expansion during dissociation translates into high excess fluid pressure when expansion is constrained. The dissociation rate is proportional to the specific surface area of the hydrate, and to the difference in fugacity between methane at the equilibrium pressure and at the decomposition pressure [*Kim et al.*, 1987].

Self preservation. The increase in pressure along the PT boundary during thermally-driven

dissociation under constrained volume expansion hinders further dissociation. The complementary effect takes place during dissociation under adiabatic conditions whereby the endothermic reaction leads to a decrease in temperature, which slows hydrate dissociation.

In addition, if the temperature drops below 273 K, ice forms on the outer surface of dissociating hydrate further preserving the encapsulated hydrate phase. The ice shield is particularly effective between 240 K and 273 K—at atmospheric pressure—as the new hexagonal ice is able to anneal This serves to heal defects and stacking faults, and gas transport is thereby severely diminished [*Stern et al.*, 2001; *Kuhs et al.*, 2004; *Circone et al.*, 2005]. Isochoric, adiabatic and the ice-shield self-preservation responses aid sample recovery from natural hydrate-bearing sediments in both standard and pressure coring operations, and may hinder methane production (e.g., see *Moridis and Sloan*, 2006).

Beyond hydrate dissociation. Water (with dissolved gas), free gas (with water vapor), and the mineral phase remain once the gas hydrate has completely dissociated. Thereafter, an additional increase in temperature under constrained volume expansion causes an increase in pressure, which is induced by the thermal expansion of the phases (C-to-D in Figure 1).

P and T dependent volume change in the phases. Thermal and pressure induced volumetric strains take place in all components throughout the different stages of heating (A-to-B, B-to-C, and C-to-D).

P-dependent global volume change. Excess pore pressure generation implies a decrease in

effective stress and expansion of the sediment skeletal structure, i.e., an increase in the total volume of the sediment. Temperature itself has a very small effect on the skeletal volume.

Phase boundary for hydrate in small pores. Water is thermodynamically preferred over the hydrate phase on mineral surfaces. Therefore, water wets the mineral surface at the hydrate-water interface and encloses the hydrate mass within a concave surface, which exerts an additional confinement $\Delta P = 2\gamma / r$ beyond the fluid pressure (where γ is the interfacial tension between hydrate and water, and r is the pore size in radius). The higher pressure in the hydrate mass does not mean stability to higher temperatures. On the contrary, the mineral preference for water prevails, water activity decreases, and there is a shift in the hydrate phase boundary towards lower temperatures, i.e., freezing/melting point depression, which is most noticeable in small pores (see data in *Uchida et al.*, 2002 and *Anderson et al.*, 2003b; discussion in *Christenson*, 2001).

3. Analytical Formulation

The evolution of the pore fluid pressure during gas hydrate dissociation in sediments is analyzed in detailed next, taking into consideration the phenomena described above. We relax some of the a-priori assumptions made in previous studies and seek to derive general expressions that facilitate identifying the interplay among various parameters and processes. In particular, we take into consideration dissolved gas, the stiffness of the sediment (related to depth of sediments and effective stress), and the volume change in all phases as a

function of temperature and pressure (parameters are listed in Table 1).

Hydrate and water—without a free gas phase—are in equilibrium within the stability zone above the base of the stability zone [*Handa*, 1990; *Clennell et al.*, 1999]. However, water-limited conditions may be locally encountered in natural sediments subjected to high gas transport. Therefore, the generic formulation developed next includes all phases: gas, water, hydrate, and mineral.

Assumptions and Governing Equations. The P and T dependent volume change in mineral, water, and hydrate phases is computed assuming an additive contribution of thermal and elastic deformations (Table 2):

$$\begin{aligned} \mathrm{dV} &= \mathrm{dP}\left(\frac{\partial \mathrm{V}}{\partial \mathrm{P}}\right)_{\mathrm{T}} + \mathrm{dT}\left(\frac{\partial \mathrm{V}}{\partial \mathrm{T}}\right)_{\mathrm{P}} \\ &= \mathrm{dP}\left(-\frac{1}{\mathrm{B}}\cdot \mathrm{V}_0\right) + \mathrm{dT}\left(\beta \cdot \mathrm{V}_0\right) \end{aligned} \tag{1}$$

The response of real materials for large P and T changes deviates from the additive rule; however, this simple assumption helps identify their separate contributions. Alternatively, empirically determined $\rho = f\left(P,T\right)$ functions can be used instead. Note that there is partial cancellation between thermal expansion and elastic contraction of the phases during thermal stimulation.

The pore water is assumed to be gas saturated, and the solubility of gas in water is computed using Henry's law. We disregard the solubility of water vapor in gas (the water vapor pressure is much smaller than the methane gas pressure), and the density change of

water due to the dissolved gas.

The mass of each species is conserved within the boundaries; that is, we assume no material flux during the thermal stimulation of the hydrate-bearing sediments. In particular, the total mass of hydrate-forming gas (HFG) remains constant:

$$\begin{aligned} n^{HFG} &= n_{h0}^{HFG} + n_{aq0}^{HFG} + n_{g0}^{HFG} \qquad \textit{initial} \\ &= n_{h}^{HFG} + n_{aq}^{HFG} + n_{g}^{HFG} \qquad \textit{after some dissociation} \end{aligned} \tag{2}$$

The moles of hydrate-forming gas n^{HFG} in each phase are captured using expressions listed in Table 3.

The total volumetric expansion of the hydrate-bearing sediment is the sum of the volume change experienced by each constituent, and is equal to the volume expansion of the granular skeleton associated with the increase in pore fluid pressure. As the effective stress $\sigma' = \sigma_{tot} - P$, the change in effective stress for a constant overburden is $-\Delta\sigma' = \Delta P$; then the volumetric strain is

$$\begin{aligned} \varepsilon &= \frac{-\Delta\sigma'}{B_{sk}} = \frac{\Delta V_t}{V_{t0}} \\ &= \frac{\Delta P}{B_{sk}} = \frac{\Delta V_m}{V_{t0}} + \frac{\Delta V_h}{V_{t0}} + \frac{\Delta V_w}{V_{t0}} + \frac{\Delta V_g}{V_{t0}} \end{aligned} \tag{3}$$

Conditions before and after partial dissociation. The sediment has an initial porosity $\phi = \mathrm{V_{pore}} / \mathrm{V_{t0}}$. The hydrate phase is in equilibrium before heating ($P_0 = P_{eq}^{T_0}$, T_0), and it occupies a pore volume fraction S_{h0}; water S_{w0} and free gas S_{g0} fill the rest of the pore

volume so that $S_{h0} + S_{w0} + S_{g0} = 1$. The initial volume of each phase is expressed as a function of volume fractions in Table 4-a.

Gas hydrate partially dissociates during heating (i.e., $-\Delta M_h$, $T = T_0 + \Delta T$), contributing both water to the water phase and gas to the gas phase (Note: The sign of ΔM_h is negative during dissociation). The final volume and corresponding volume change for each phase after partial dissociation are given in Table 4-b. Initial and final masses are summarized in Table 4-c.

General Equation. Expressions in Table 4 are replaced into Equation 3 to obtain a general expression:

$$\begin{aligned}\varepsilon = &\left(1-\phi\right)\varepsilon_m \\ &+\phi\left(S_{h0}\varepsilon_h + S_{w0}\varepsilon_w\right) \\ &+\frac{\Delta M_h}{V_{t0}}\left[\frac{1+\varepsilon_h}{\rho_{h0}} - \frac{\left(1+\varepsilon_w\right)\left(1-R_m\right)}{\rho_{w0}}\right] \\ &+\frac{\Delta V_g}{V_{t0}}\end{aligned} \tag{4}$$

The last term $\Delta V_g / V_{t0}$ is the volume change of gas normalized by the initial volume of the hydrate-bearing sediment. It can be expressed as follows:

$$\frac{\Delta V_g}{V_{t0}} = \frac{n_g^{HFG} RT}{PV_{t0}} - \phi \cdot S_{g0} \tag{5}$$

Then, we replace n_g^{HFG} by equations in Table 3 to obtain

$$\frac{\Delta V_g}{V_{t0}} = \frac{\Delta M_h}{V_{t0}} RT \left[\left(1+\varepsilon_w\right) k_H^T \frac{1-R_m}{\rho_{w0}} - \frac{1}{m_h P} \right] + \phi S_{w0} RT \left[k_H^{T_0} \frac{P_0}{P} - \left(1+\varepsilon_w\right) k_H^T \right] + \phi S_{g0} \left(\frac{T}{T_0} \frac{P_0}{P} - 1 \right) \quad (6)$$

As long as hydrate remains in the system, the pressure P for a given temperature T is the corresponding equilibrium pressure P_{eq}^T on the phase boundary. The increase in pressure ΔP_{final} when all the hydrate in the system is consumed can be evaluated using Equations 4-to-6 for $\Delta M_h = -M_{h0}$.

Volumetric fractions during thermal stimulation. Volumetric and gravimetric quantities of any phase can be evaluated using the equations in Table 4, including the molar quantity of methane in the gas phase or the volume fraction of free gas in pores. These quantities help assess the evolution of the system during dissociation; for example, the volume fraction of free gas S_g relative to the gas percolation threshold plays a critical role on multiphase flow in porous media, such as reservoirs.

Of particular interest is the hydrate mass change ΔM_h during dissociation (BC path in Figure 1). It can be computed using Equations 4-to-6 for a given PT state on the phase boundary (P_{eq}^T, T). The remaining gas hydrate volume fraction S_h is related to ΔM_h through the mass density, with proper consideration of volumetric strains

$$S_h\left(\Delta M_h\right)=\frac{\left(\phi\cdot S_{h0}+\dfrac{\Delta M_h}{\rho_{h0}V_{t0}}\right)\left(1+\varepsilon_h\right)}{\left(1+\dfrac{\Delta P}{B_{sk}}\right)-\left(1-\phi\right)\left(1+\varepsilon_m\right)} \tag{7}$$

4. Discussion – Implications

4.1. Initial hydrate and gas fractions.

Thermal stimulation of hydrate-bearing sediments can cause a very large increase in the fluid pressure within sediments under constrained volume expansion with high skeletal stiffness B_{sk}. Numerical results in Figure 2 show that the excess fluid pressure during partial dissociation is primarily determined by the increase in temperature, while the excess fluid pressure after complete dissociation is strongly dependent on the initial volume fractions of hydrate S_{h0} and free gas S_{g0}. The existence of a gas phase acts as a cushion against the pressure increase, diminishes self preservation and allows for faster gas hydrate dissociation with increasing temperature (Figure 2b). In the absence of fluid flux, a significantly high increase in temperature would be required to attain complete dissociation.

Experimental data were gathered with a transparent reaction cell (volume 3.17 cm^3; internal diameter 6.35 mm; height 100 mm) packed with water saturated sand at a porosity ϕ = 0.4 (Ottawa F110; uniform grain size; mean diameter = 0.1 mm). Water and CO_2 gas were sequentially flushed through the specimen (P = 3.2 MPa and T = 2°C) and left to stabilize for 3 days. Then, the cell was slowly heated at 0.5°C/hour without allowing fluid flux. The

measured temperature and pressure evolution denoted as Test 1 in Figure 3 was fitted with the analytical solution to infer the initial volume fractions in the system: S_{h0} = 5%, S_{w0} = 16%, S_{g0} = 79%. The high pressure that develops during hydrate dissociation can cause liquefaction of CO_2; Test 2 demonstrates this situation (Figure 3 – Note: the model can be readily extended to accommodate gas liquefaction).

4.2. Effective stress and sediment stiffness – depth effect.

The stiffness of uncemented sediments is determined by the effective stress $B_{sk} = \alpha(\sigma')^{\beta}$ [*Santamarina et al.*, 2001]. Accordingly, low stiffness shallow sediments will experience larger volumetric deformation and lower excess pore pressure than the same sediments at greater depth, as shown in Figure 4. Still, high excess fluid pressures are anticipated.

Eventually, the fluid pressure is limited by the effective stress dependent sediment failure boundary. The red and blue dash lines superimposed on Figure 4a indicate the extent of dissociation when the excess pore pressure equals the initial effective stress, i.e., "soil liquefaction". Low initial effective stress corresponds to low skeletal stiffness and decreased pore pressure generation during dissociation; however, it also implies low pore pressure required to reach failure. In fact, shallow sediments fail at lower hydrate dissociation than do deep sediments. Non-plastic soils develop higher bulk stiffness than plastic soils at the same effective stress. Therefore, sandy soils could reach failure conditions before clayey sediments; however, effective fluid flow in sands with high hydraulic conductivity leads to the opposite trend in most field situations. Uncemented

sediments in the upper 1000 mbsf may reach failure conditions with less than 6% hydrate dissociation in the absence of a gas phase and fluid flux.

4.3. Shallow Sediments – Simplification.

Low sediment stiffness in shallow formations and partial cancellation between thermal expansion and elastic contraction of the phases during thermal stimulation can be invoked to obtain the following simplified form of Equation 4:

$$\varepsilon = \frac{\Delta M_h}{V_{t0}}\left[\frac{1}{\rho_{h0}} - \frac{1-R_m}{\rho_{w0}}\right] + \frac{\Delta V_g}{V_{t0}} \tag{8}$$

As a general guideline, this simplification is valid when the sediment bulk stiffness is B_{sk} < 1 GPa, which typically includes uncemented sediments in the upper 1000 mbsf.

4.4. Changes in density.

Pore pressure generation is affected by density changes in the components in stiff formations with high hydrate volume fraction, as shown in Figure 5 (i.e., B_{sk} > 1GPa). Otherwise, the simplified Equation 8 applies.

4.5. Dissolved gas.

The solubility of gas in water can have a distinct effect on excess pore pressure generation in stiff systems (Figure 5). The effect of gas solubility in water is highlighted by comparing the excess pore pressure produced by the dissociation of carbon dioxide CO_2 and methane hydrates (Figure 6 – Note: CO_2 is ~10 times more soluble in water than CH_4). The

reduction in excess fluid pressure generation by gas dissolution in water should not be disregarded a priori for all applications. In particular, the dissociation of CO_2 hydrate may produce less than one-third the excess pore pressure generated by CH_4 hydrate dissociation.

4.6. Pore size – Capillarity.

Capillarity in fine-grained sediments manifests through two mechanisms: freezing-melting point depression and increased gas pressure. First, the melting point depression ΔT_{dep} from the equilibrium temperature in unconfined conditions T_{bulk} is computed using the Gibbs-Thomson equation with consideration of the total curvature of the solid surface in terms of the effective pore size d [*Everett*, 1961; *Williams and Smith*, 1989; *Jallut et al.*, 1992; *Anderson et al.*, 2003a].

$$\Delta T_{dep} = -\frac{2}{d}\left(\frac{\gamma_{hw} m_h \cos\theta}{\rho_{h0} L_f}\right) T_{bulk} \qquad \text{Cylindrical hydrate shape} \qquad (9a)$$

$$\Delta T_{dep} = -\frac{4}{d}\left(\frac{\gamma_{hw} m_h \cos\theta}{\rho_{h0} L_f}\right) T_{bulk} \qquad \text{Spherical hydrate shape} \qquad (9b)$$

where L_f is the latent heat of dissociation of gas hydrate (53.2 kJ/mol from *Anderson et al.*, 2003b), and γ_{hw} is the surface tension between methane hydrate and water (~0.032 N/m after *Uchida et al.*, 1999 and *Anderson et al.*, 2003b; and for ice in *Clennell et al.*, 1999). Capillary effects on excess pore pressure generation along the phase boundary are shown in Figure 7, where the analytical solution is superimposed on previously published experimental data (we disregard changes in pore size during dissociation and consider the

contact angle between the water and the pore wall to be $\theta = 0$ by assuming that minerals are coated by a water film). The results suggest that the hydrate surface can be presumed to be cylindrical when gas hydrate occupies most of the pore space (solid lines denoted as CYL in Figure 7). On the other hand, disseminated gas hydrate crystals may be encapsulated by spherical water films and experience higher capillary pressure and melting point depression (dash lines denoted as SPH in Figure 7). Therefore, the dissociation temperature for a given pore size is affected by the hydrate fraction.

Second, the increase in gas pressure inside spherical bubbles P_g relative to the surrounding water pressure P_w is computed using Laplace's equation to take into consideration the additional confinement exerted by the surface tension between gas and water $\gamma_{gw} \sim 0.072$ N/m [*Clennell et al.*, 1999],

$$P_g = P_w + \frac{2\gamma_{gw}}{r} = P_w + \frac{4\gamma_{gw}}{d} \tag{10}$$

Figure 8 shows the pressure and temperature evolution of disseminated gas hydrate with 20% of hydrate fraction in pores. The water pressure evolves along the shifted phase boundary (Figure 8a). The pressure at the end of dissociation decreases in finer sediments due to the smaller volume occupied by the gas phase subjected to higher pressures in small bubbles (Figure 8b).

The effects of pore size on melting point depression and pressure reduction vanish as pores exceed ~100 nm. Therefore, sands, silts and even kaolinites do not experience capillary

effects. On the other, one should expect pronounced capillary effects in very fine clays, such as illite and montmorillonite, where the excess pore pressure may be as low as half the value of that in sands. However, capillary effects will vanish when hydrates are found in nodules, veins, and lenses, and when the high excess pore pressure causes the hydraulic fracture of the sediment, which is associated with a large increase in local pore size.

5. Conclusions

A comprehensive analytical solution was derived to explore the evolution of hydrate-bearing sediments during thermal stimulation, with an emphasis on excess pore pressure generation under constrained volume conditions in the absence of fluid flux. The formulation captures the effects of sediment stiffness, the cushioning effect of an initial gas phase, change in the density of the phases, variation in gas solubility, the relevance of initial hydrate content, and capillary effects. The most important findings are as follows:

- Partial dissociation during thermal stimulation is characterized by a pressure-temperature evolution along the phase boundary until all hydrate has dissociated. Higher gas hydrate concentration causes higher fluid pressure generation during dissociation and extends self preservation behavior during thermal stimulation. In addition to fluid flux, the presence of a gas phase, low skeletal stiffness and capillary effects reduce pressure generation.

- Eventually, excess fluid pressure generation is limited by failure conditions. For a given

hydrate concentration, lower excess pore pressure generation develops in shallow sediments due to lower sediment stiffness. However, shallower sediments require lower amounts of hydrate dissociation to reach failure than do deeper sediments, and hence they need a smaller increase in temperature. Less than 6% volume fraction dissociation may be sufficient to cause the failure of uncemented sediments in the upper 1000 mbsf, in the absence of fluid flux.

- Thermal and pressure induced density changes in water, hydrate, and mineral can be disregarded in most applications (uncemented sediments in the upper 1000 mbsf), except in deep sediments with high initial stiffness.

- Gas solubility in water diminishes pore pressure generation. The reduction in excess fluid pressure generation by gas dissolution in water should not be disregarded a priori for all applications. For example, the dissociation of CO_2 hydrate may produce less than one-third the excess pressure that is generated by CH_4 hydrate dissociation.

- Hydrate dissociation in small pores is affected by melting point depression and lower fluid pressure generation due to the additional confinement the water-gas interface exerts on small gas bubbles. Therefore, lower excess pore water pressure develops in finer sediments with disseminated hydrates. Capillary effects vanish when pores exceed ~100 nm (sands and silts), when hydrates are present in nodules and lenses, and after the development of hydraulic fractures.

Acknowledgements

Support for this research was provided by grant No. (R01-2006-000-10727-0) from the Basic Research Program of the Korea Science & Engineering Foundation and by the DOE Joint Industry Project for Methane Hydrate administered by ChevronTexaco.

References

Anderson, R., M. Llamedo, B. Tohidi, and R. W. Burgass (2003a), Characteristics of clathrate hydrate equilibria in mesopores and interpretation of experimental data, *J. Phys. Chem. B*, *107*, 3500-3506.

Anderson, R., M. Llamedo, B. Tohidi, and R. W. Burgass (2003b), Experimental measurement of methane and carbon dioxide clathrate hydrate equilibria in mesoporous silica, *J. Phys. Chem. B*, *107*, 3507-3514.

Aya, I., K. Yamane, and H. Nariai (1997), Solubility of CO_2 and density of CO_2 hydrate at 30 MPa, *Energy*, *22*, 263-271.

Birchood, R., S. Noeth, and P. Hooyman (2005), Wellbore stability model for marine sediments contanining gas hydrates, paper presented at AADE 2005 National Technical Conference and Exhibition, Houston, USA.

Briaud, J. L., and A. Chaouch (1997), Hydrate melting in soil around hot conductor, *J. Geotech. Geoenviron. Eng.*, *123*, 645-653.

Christenson, H. K. (2001), Confinement effects on freezing and melting, *J. Phys.-Condes. Matter*, *13*, R95-R133.

Circone, S., S. H. Kirby, and L. A. Stern (2005), Thermal regulation of methane hydrate dissociation: Implications for gas production models, *Energy Fuels*, *19*, 2357-2363.

Clennell, M., M. Hovland, J. S. Booth, P. Henry, and W. J. Winters (1999), Formation of natural gas hydrates in marine sediments 1. Conceptual model of gas hydrate growth conditioned by host sediment properties, *J. Geophys. Res.*, *104*, 22985-23003.

Davie, M. K., O. Y. Zatsepina, and B. A. Buffett (2004), Methane solubility in marine hydrate environments, *Mar. Geol.*, *203*, 177-184.

Dillon, W. P., and M. D. Max (2000), Oceanic Gas Hydrate, *M.D. Max (ed.), Natural Gas Hydrate in Oceanic and Permafrost Environments*, 61-76.

Duan, Z. H., and S. D. Mao (2006), A thermodynamic model for calculating methane solubility, density and gas phase composition of methane-bearing aqueous fluids from 273 to 523 K and from 1 to 2000 bar, *Geochim. Cosmochim. Acta*, *70*, 3369-3386.

Everett, D. H. (1961), Thermodynamics of frost damage to porous solids, *Transactions of the Faraday Society*, *57*, 1541-1551.

Handa, Y. P. (1990), Effect of hydrostatic pressure and salinity on the stability of gas hydrates, *J. Phys. Chem.*, *94*, 2652-2657.

Handa, Y. P., and D. Stupin (1992), Thermodynamic properties and dissociation characteristics of methane and propane hydrates in 70-Angstrom-radius silica-gel pores, *J. Phys. Chem.*, *96*, 8599-8603.

Holder, G. D., V. A. Kamath, and S. P. Godbole (1984), The potential of natural gas hydrates as an energy resource, *Annual Review of Energy*, *9*, 427-445.

HWHYD (2001). A demo version of this software is available at http://www.pet.hw.ac.uk/research /hydrate.

Jallut, C., J. Lenoir, C. Bardot, and C. Eyraud (1992), Thermoporometry - Modeling and simulation of a mesoporous solid, *J. Membr. Sci.*, *68*, 271-282.

Kayen, R. E., and H. J. Lee (1991), Pleistocene slope instability of gas hydrate-laden sediment on the Beaufort sea margin, *Mar. Geotechnol., 10*, 125-141.

Kim, H. C., P. R. Bishnoi, R. A. Heidemann, and S. S. H. Rizvi (1987), Kinetics of methane hydrate decomposition, *Chem. Eng. Sci.*, *42*, 1645-1653.

Kuhs, W. F., G. Genov, D. K. Staykova, and T. Hansen (2004), Ice perfection and onset of anomalous preservation of gas hydrates, *Phys. Chem. Chem. Phys.*, *6*, 4917-4920.

Lide, D. R. (1997), *CRC Handbook of Chemistry and Physics*, 78th Edition ed., **8**-81 pp., CRC Press Inc., Boca Raton, FL.

Marshall, D. R., S. Saito, and R. Kobayashi (1964), Hydrates at high pressures: Part 1. Methane-water, argon-water, and nitrogen-water systems, *AIChE. J.*, *10*, 202-205.

Moridis, G. J. (2003), Numerical studies of gas production from methane hydrates, *SPE J.*, *December*, 359-370.

Moridis, G. J., and E. D. Sloan (2006), Gas production potential of disperse low-saturation hydrate accumulations in oceaninc sediments, U.S. Department of Energy, report LBNL 61446.

Nixon, M. F., and J. L. H. Grozic (2007), Submarine slope failure due to gas hydrate dissociation: a preliminary quantification, *Can. Geotech. J.*, *44*, 314-325.

Osegovic, J. P., S. R. Tatro, and S. A. Holman (2006), Physical Chemical Characteristics of Natural Gas Hydrate, *Max, M. D., Johnson, A.H. and Dillon, W. P. (ed.) Economic Geology of Natural Gas Hydrate*, 45-104.

Pawar, R. J., G. A. Zyvoloski, N. Tenma, Y. Sakaoto, and T. Komai (2005), Numerical simulation of

gas production from methane hydrate reservoirs, paper presented at The fifth international conference on gas hydrates, Trondheim, Norway, June 12-16, 2005.

Santamarina, J. C., K. A. Klein, and M. A. Fam (2001), Soils and Waves, *John Wiley & Sons, Ltd., England.*

Schroeter, J. P., R. Kobayashi, and M. A. Hildebrand (1983), Hydrate decomposition conditions in the system H_2S-methane-propane, *Ind. Eng. Chem. Fundamentals*, *22*, 361-364.

Servio, P., and P. Englezos (2001), Effect of temperature and pressure on the solubility of carbon dioxide in water in the presence of gas hydrate, *Fluid Phase Equilib.*, *190*, 127-134.

Sloan, E. D. (1998), Clathrate hydrates of natural gas, 2nd Ed., *Dekker, New York*.

Stern, L. A., S. Circone, S. H. Kirby, and W. B. Durham (2001), Anomalous preservation of pure methane hydrate at 1 atm, *J. Phys. Chem. B*, *105*, 1756-1762.

Sultan, N. (2007), Comment on "Excess pore pressure resulting from methane hydrate dissociation in marine sediments: A theoretical approach" by Wenyue Xu and Leonid N. Germanovich, *J. Geophys. Res.*, *112*, B102103, doi:10.1029/2006JB004527.

Sultan, N., P. Cochonat, J. P. Foucher, and J. Mienert (2004), Effect of gas hydrates melting on seafloor slope instability, *Mar. Geol.*, *213*, 379-401.

Uchida, T., T. Ebinuma, and T. Ishizaki (1999), Dissociation condition measurements of methane hydrate in confined small pores of porous glass, *J. Phys. Chem. B*, *103*, 3659-3662.

Uchida, T., T. Ebinuma, S. Takeya, J. Nagao, and H. Narita (2002), Effects of pore sizes on dissociation temperatures and pressures of methane, carbon dioxide, and propane hydrates in porous

media, *J. Phys. Chem. B*, *106*, 820-826.

Ullerich, J. W., M. S. Selim, and E. D. Sloan (1987), Theory and measurement of hydrate dissociation, *AIChE J.*, *33*, 747-752.

Williams, P. J., and M. W. Smith (1989), *The Frozen Earth - Fundamentals of Geocryology*, 185-193 pp., Cambridge Press.

Xu, W. Y., and L. N. Germanovich (2006), Excess pore pressure resulting from methane hydrate dissociation in marine sediments: A theoretical approach, *J. Geophys. Res.*, *111*, B01104, doi:01110.01029/02004JB003600.

Xu, W. Y., and L. N. Germanovich (2007), Reply to comment by Nabil Sultan on "Excess pore pressure resulting from methane hydrate dissociation in marine sediments: A theoretical approach", *J. Geophys. Res., 112*, B02104, doi:02110.01029/02006JB004722.

Table 1. Parameters used in this study.

Parameter	Definition [Dimension]	Values selected for this study
B	Bulk modulus [GPa]	
B_h	of gas hydrate	5.6 for methane hydrate [a]
B_w	of water	2 [b]
B_m	of minerals	67 for quartz [b]
B_{sk}	of sediments	-
d	pore size in diameter [m]	
$\Delta H_{solution}$	Enthalpy of the solution [J mol^{-1}]	-39580 for CH_4 [c] and -19960 for CO_2 [d]
k_H^T	Gas solubility at temperature T Henry's law [mol L^{-1} atm^{-1}]	$k_H^T = k_H^o \cdot \exp\left[\frac{-\Delta H_{solution}}{R}\left(\frac{1}{T} - \frac{1}{T_{298.15K}}\right)\right]$
k_H^o	Henry's constant at 298 K [mol m^{-3} atm^{-1}]	0.599 for CH_4 [c] and 35 for CO_2 [d]
L_f	Latent heat of dissociation [kJ mol^{-1}]	53.2 [e] for methane hydrate
m	Molecular weight [g mol^{-1}]	
m_h	of gas hydrate	119.5 for $CH_4 \cdot 5.75H_2O$
m_w	of water	18
n^{HFG}	Mole of hydrate-forming gas [mole]	
n_h	in hydrate phase	
n_{aq}	in aqueous phase	
n_g	in gas phase	
P	Fluid pressure – gas or water [Pa]	
P_{eq}^T	Equilibrium pressure on the hydrate stability boundary at temperature T	$P_{eq}^T\,[\mathrm{kPa}] = \exp\left(a + b/T\,[\mathrm{K}]\right)$ a=40.234, b= –8860 for CH_4 [f] a=41.235, b= –9317 for CO_2 [f]
R	Gas constant [J mol^{-1} K^{-1}]	8.315
S	Volume fraction in pores [-]	$S_{h0} + S_{w0} + S_{g0} = 1$
S_h	of gas hydrate	$S_{h0} = V_{h0} / V_{p0}$
S_w	of water	$S_{w0} = V_{w0} / V_{p0}$
S_g	of free gas	$S_{g0} = V_{g0} / V_{p0}$
T	Absolute temperature [K]	
V	Volume [m^3]	
β	Thermal expansivity [K^{-1}]	$\Delta V = \beta \Delta T V_0$
β_h	of gas hydrate	2.57x10^{-5} for methane hydrate [a]
β_w	of water	2.0x10^{-4} [b]
β_m	of minerals	2.1x10^{-4} [b]
γ	Surface tension [N/m]	0.032 [e] for water-hydrate interface 0.072 [d, g] for water-gas interface
ε	Volumetric strain [-]	
ϕ	Porosity of the sediment [-]	
ρ	Mass density [kg m^{-3}]	
ρ_h	of gas hydrate	910 for methane hydrate [a]
ρ_w	of water	998 for pure water [b]
χ	Hydration number [-]	5.75 for methane hydrate [a]

References: a. *Sloan* [1998]; b. *Santamarina et al.* [2001]; c. The solubility coefficients for methane are modified

using data from *Duan and Mao* [2006]; d. *Lide* [1997]; e. *Anderson et al* [2003b]; f. The expressions for the phase boundary of methane hydrate and CO_2 hydrate from *Sloan* [1998] are modified using data computed with *HWHYD software* [2001]; g. *Clennell et al.* [1999].

Table 2. Density as a function of temperature and pressure.

Phase	Initial density (at P_0 and T_0)	Density (at P and T)	Volumetric strain
Mineral	ρ_{m0}	$\rho_m = \frac{\rho_{m0}}{1+\varepsilon_m}$	$\varepsilon_m = -\frac{\Delta P}{B_m} + \beta_m \Delta T$
Hydrate	ρ_{h0}	$\rho_h = \frac{\rho_{h0}}{1+\varepsilon_h}$	$\varepsilon_h = -\frac{\Delta P}{B_h} + \beta_h \Delta T$
Water	ρ_{w0}	$\rho_w = \frac{\rho_{w0}}{1+\varepsilon_w}$	$\varepsilon_w = -\frac{\Delta P}{B_w} + \beta_w \Delta T$

Table 3. Hydrate-forming gas HFG content in each phase before and after dissociation – In moles.

Phase	Before dissociation (at P_0 and T_0)	After partial dissociation (at P and T)
Hydrate phase	$n_{h0}^{HFG} = \frac{M_{h0}}{m_h}$	$n_h^{HFG} = \frac{M_{h0} + \Delta M_h}{m_h}$
Aqueous phase	$n_{aq0}^{HFG} = k_H^{T_0} \cdot P_0 \cdot V_{w0}$	$n_{aq}^{HFG} = k_H^T \cdot P \cdot V_w$
Gas phase	$n_{g0}^{HFG} = \frac{P_0 \cdot V_{g0}}{R \cdot T_0}$	n_g^{HFG} from mass conservation: $0 = n_{h0}^{HFG} + n_{g0}^{HFG} + n_{aq0}^{HFG} - n_h^{HFG} - n_g^{HFG} - n_{aq}^{HFG}$

(Note that the P-T state falls on the phase equilibrium after partial dissociation, i.e., $P_0 = P_{eq}^{T_0}$, and $P = P_{eq}^{T}$.)

Table 4. Volume, volume change and mass before and after partial dissociation.

(a)	Initial volume (at P_0 and T_0)	Volume after partial dissociation (at P and T)
Mineral	$V_{m0} = (1-\phi)\cdot V_{t0}$	$V_m = \dfrac{M_{m0}}{\rho_m}$
Hydrate	$V_{h0} = \phi \cdot S_{h0} \cdot V_{t0}$	$V_h = \dfrac{M_{h0} + \Delta M_h}{\rho_h}$
Water	$V_{w0} = \phi \cdot (1 - S_{h0} - S_{g0}) \cdot V_{t0}$	$V_w = \dfrac{M_{w0} - \Delta M_h (1 - R_m)}{\rho_w}$
Gas	$V_{g0} = \phi \cdot S_{g0} \cdot V_{t0}$	$V_g = \dfrac{n_g^{HFG} RT}{P}$
(b)	Volume change from (P_0, T_0) to (P, T)	
Mineral	$\Delta V_m = (1-\phi)\cdot V_{t0} \cdot \varepsilon_m$	
Hydrate	$\Delta V_h = \phi \cdot S_{h0} \cdot V_{t0} \cdot \varepsilon_h + \dfrac{\Delta M_h}{\rho_{h0}}(1 + \varepsilon_h)$	
Water	$\Delta V_w = \phi \cdot (1 - S_{h0} - S_{g0}) \cdot V_{t0} \cdot \varepsilon_w - \dfrac{\Delta M_h}{\rho_{w0}} \cdot (1 + \varepsilon_w) \cdot (1 - R_m)$	
Gas	$\Delta V_g = \dfrac{n_g^{HFG} RT}{P} - \phi \cdot S_{g0} \cdot V_{t0}$	
(c)	Initial mass (at P_0 and T_0)	Mass after partial dissociation (at P and T)
Mineral	$M_{m0} = (1-\phi)\cdot V_{t0} \cdot \rho_{m0}$	$M_m = M_{m0}$
Hydrate	$M_{h0} = \phi \cdot S_{h0} \cdot V_{t0} \cdot \rho_{h0}$	$M_h = M_{h0} + \Delta M_h$
Water	$M_{w0} = \phi \cdot (1 - S_{h0} - S_{g0}) \cdot V_{t0} \cdot \rho_{w0}$	$M_w = M_{w0} - \Delta M_h \cdot (1 - R_m)$

(Note that the P-T state falls on the phase equilibrium after partial dissociation, i.e., $P_0 = P_{eq}^{T_0}$, and $P = P_{eq}^{T}$.)

Figure Captions

Figure 1. Pressure and temperature evolution during thermal stimulation. L_W: liquid water. H: hydrate. V: CH_4 in vapor phase. The phase boundary *PB* shown corresponds to pure methane hydrate in Table 1: P [kPa] = exp (40.234 – 8860/T [K]); this expression is modified from *Sloan* [1998] using data computed with *HWHYD software* [2001].

Figure 2. Thermal stimulation of methane hydrate-bearing sediments. Initial conditions: T = 4°C, P = 4.9 MPa, and sediment stiffness B_{sk} = 100 MPa. (a) Pressure evolution (b) Change in hydrate volume fraction. Dissociation begins at temperature of 6°C. Note: *PB* represents the phase boundary of pure methane hydrate in Table 1: P [kPa] = exp (40.234 – 8860/T [K]); this expression is modified from *Sloan* [1998] using data computed with *HWHYD software* [2001].

Figure 3. Measured pressure-temperature response during isochoric heating of CO_2 hydrate. The solid line represents the theoretical prediction curve for Test 1. L_W: liquid water. H: hydrate. V_{CO2}: CO_2 in vapor phase. L_{CO2}: CO_2 in liquid phase. The phase boundaries L_W–H–V_{CO2}, H–V–L_{CO2}, L_W–V_{CO2}–L_{CO2}, and L_W–H–V_{CO2} are computed using the *HWHYD software* [2001].

Figure 4. The effect of the sediments stiffness on pressure evolution during the thermal stimulation of methane hydrate-bearing sediments. Initial condition at the beginning of dissociation: T = 6°C, P = 4.9 MPa, initial hydrate fraction S_{h0} = 20%, and initial gas fraction S_{g0} = 0%. The dashed lines show sediment failure conditions (excess pore pressure equal to the initial effective stress): the blue line applies to low plasticity soils and red line to high plasticity clayey soils. All cases computed using values listed in Table 1.

Figure 5. The effects of density changes in components and gas dissolution on pressure evolution during the thermal stimulation of methane hydrate-bearing sediments in stiff formations (B_{sk} = 10^{10} Pa). All cases computed using values listed in Table 1. Initial condition at the beginning of dissociation: T = 6°C, P = 4.9 MPa, initial hydrate fraction S_{h0} = 20%, and initial gas fraction S_{g0} = 0%.

Figure 6. Dissociation of CH_4 and CO_2 hydrates. Initial conditions: sediment stiffness B_{sk} = 100 MPa, initial hydrate fraction S_{h0} = 20%, initial gas fraction S_{g0} = 0%, initial temperature T = 6°C, and the initial equilibrium pressure for CH_4 hydrate P_{CH4} = 4.9 MPa, and for CO_2 hydrate P_{CO2} = 2.6 MPa.

Figure 7. Capillary effects on phase boundary: Pore size and pore geometry. Published data and simulations. Initial conditions: sediment stiffness B_{sk} = 100 MPa, initial hydrate fraction S_{h0} = 80%, initial gas fraction S_{g0} = 0%, initial fluid pressure at the beginning of dissociation P = 5.5 MPa for pore size d = 10 nm and P = 3.0 MPa for pore size d = 30 nm. Note: The phase boundary *PB* shown corresponds to pure methane hydrate in unconfined sediments in Table 1: P [kPa] = exp (40.234 – 8860/T [K]); this expression is modified from *Sloan* [1998] using data computed with *HWHYD software* [2001].

Figure 8. Effect of pore size on pore pressure generation. Initial conditions: sediment stiffness B_{sk} = 100 MPa, initial hydrate fraction S_{h0} = 20%, initial gas fraction S_{g0} = 0%, initial temperature T = -3C, and the initial fluid pressure P = 4.9 MPa. (a) Pressure-temperature trace in PT plane. (b) Pressure evolution during dissociation. Note: The phase boundary *PB* shown corresponds to pure methane hydrate in unconfined sediments in Table 1: P [kPa] = exp (40.234 – 8860/T [K]); this expression is modified from *Sloan* [1998] using data computed with *HWHYD software* [2001].

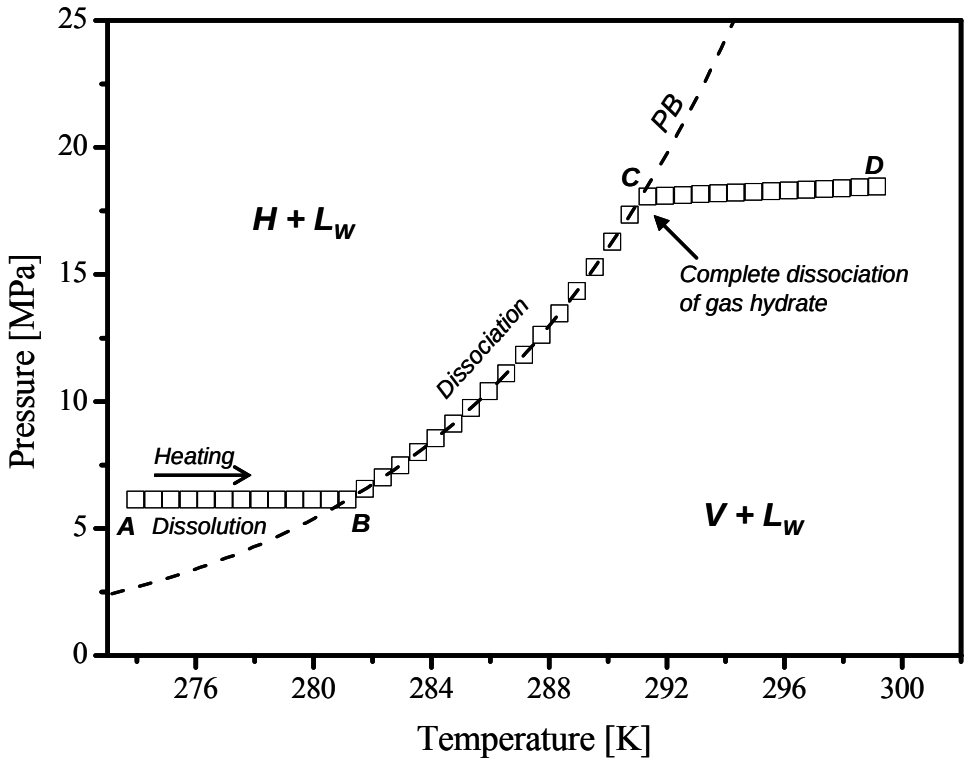

Figure 1. Pressure and temperature evolution during thermal stimulation. L_W: liquid water. H: hydrate. V: CH_4 in vapor phase. The phase boundary *PB* shown corresponds to pure methane hydrate in Table 1: P [kPa] = exp (40.234 – 8860/T [K]); this expression is modified from *Sloan* [1998] using data computed with *HWHYD software* [2001].

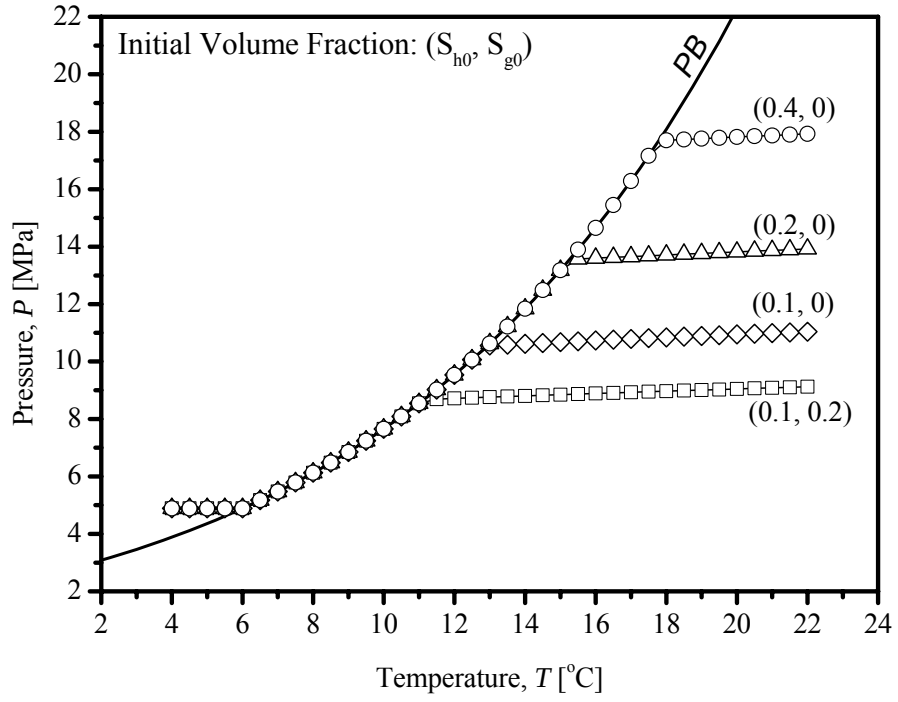

(a)

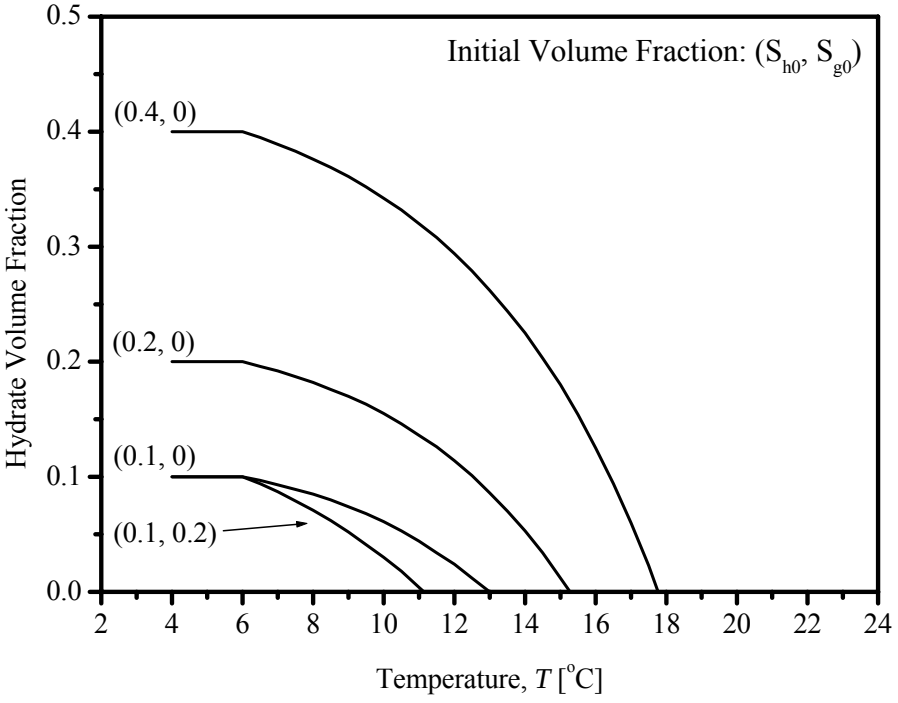

(b)

Figure 2. Thermal stimulation of methane hydrate-bearing sediments. Initial conditions: T = 4°C, P = 4.9 MPa, and sediment stiffness B_{sk} = 100 MPa. (a) Pressure evolution (b) Change in hydrate volume fraction. Dissociation begins at temperature of 6°C. Note: *PB* represents the phase boundary of pure methane hydrate in Table 1: P [kPa] = exp (40.234 – 8860/T [K]); this expression is modified from *Sloan* [1998] using data computed with *HWHYD software* [2001].

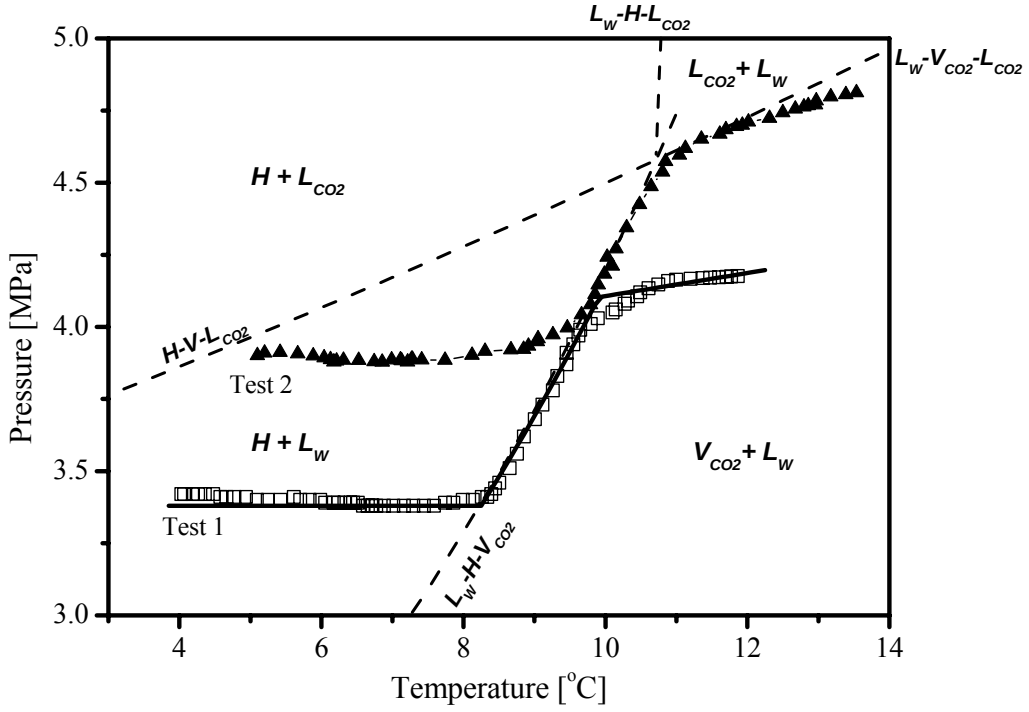

Figure 3. Measured pressure-temperature response during isochoric heating of CO_2 hydrate. The solid line represents the theoretical prediction curve for Test 1. L_W: liquid water. H: hydrate. V_{CO2}: CO_2 in vapor phase. L_{CO2}: CO_2 in liquid phase. The phase boundaries L_W–H–V_{CO2}, H–V–L_{CO2}, L_W–V_{CO2}–L_{CO2}, and L_W–H–V_{CO2} are computed using the *HWHYD software* [2001].

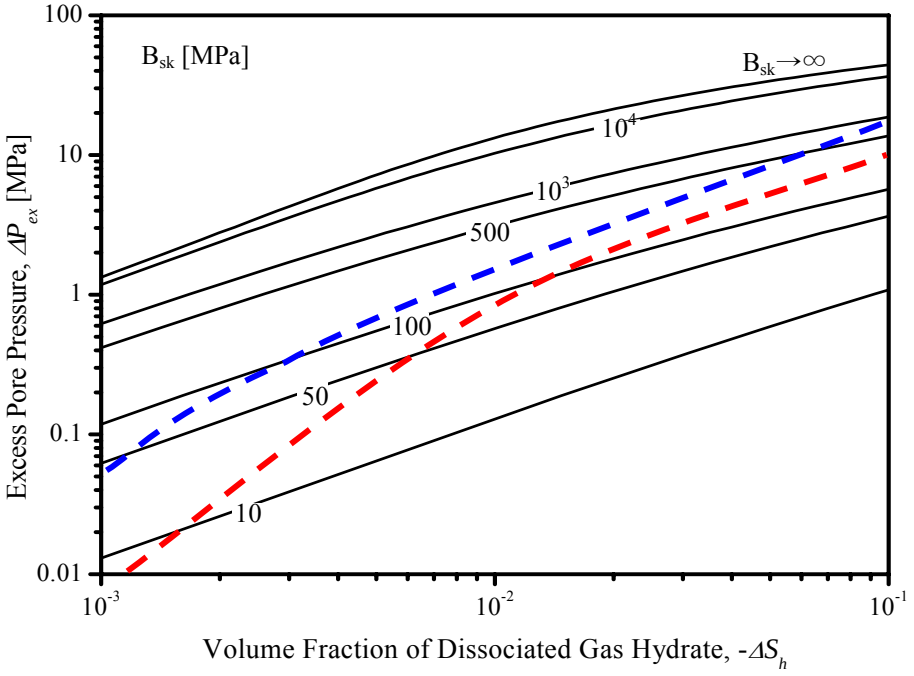

Figure 4. The effect of the sediments stiffness on pressure evolution during the thermal stimulation of methane hydrate-bearing sediments. Initial condition at the beginning of dissociation: T = 6°C, P = 4.9 MPa, initial hydrate fraction S_{h0} = 20%, and initial gas fraction S_{g0} = 0%. The dashed lines show sediment failure conditions (excess pore pressure equal to the initial effective stress): the blue line applies to low plasticity soils and red line to high plasticity clayey soils All cases computed using values listed in Table 1.

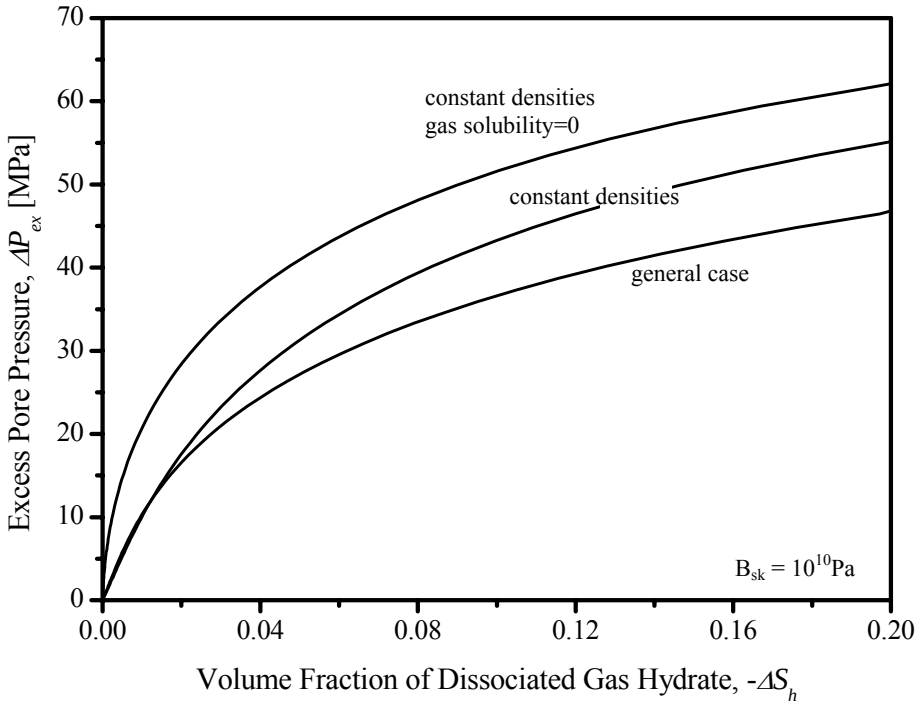

Figure 5. The effects of density changes in components and gas dissolution on pressure evolution during the thermal stimulation of methane hydrate-bearing sediments in stiff formations ($B_{sk} = 10^{10}$ Pa). All cases computed using values listed in Table 1. Initial condition at the beginning of dissociation: T = 6°C, P = 4.9 MPa, initial hydrate fraction S_{h0} = 20%, and initial gas fraction S_{g0} = 0%.

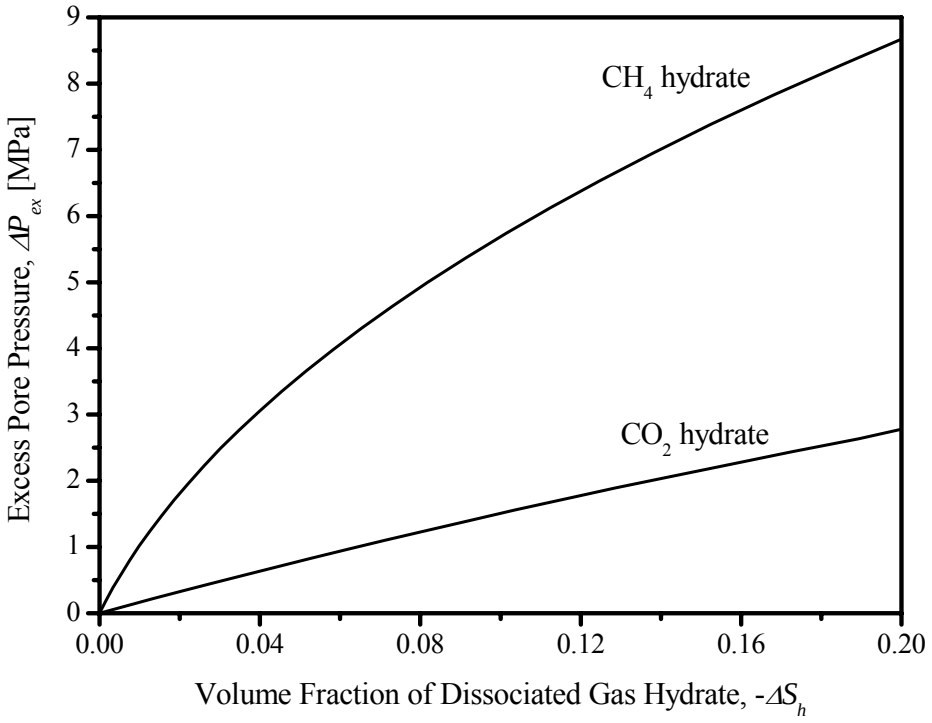

Figure 6. Dissociation of CH_4 and CO_2 hydrates. Initial conditions: sediment stiffness B_{sk} = 100 MPa, initial hydrate fraction S_{h0} = 20%, initial gas fraction S_{g0} = 0%, initial temperature T = 6°C, and the initial equilibrium pressure for CH_4 hydrate P_{CH4} = 4.9 MPa, and for CO_2 hydrate P_{CO2} = 2.6 MPa.

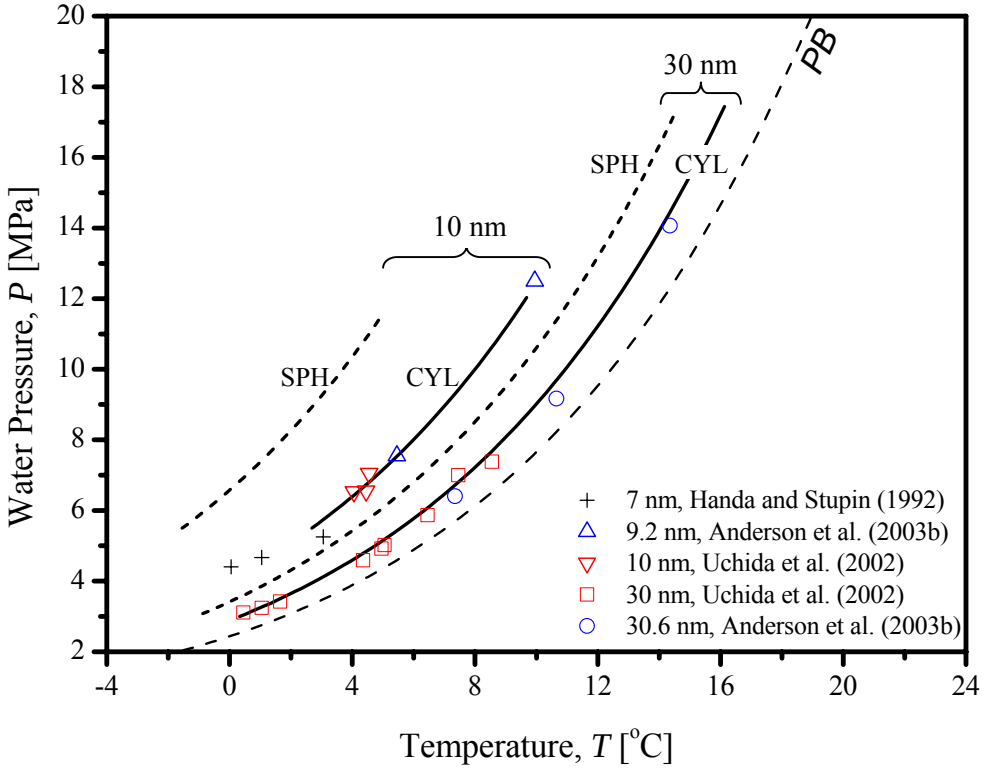

Figure 7. Capillary effects on phase boundary: Pore size and pore geometry. Published data and simulations. Initial conditions: sediment stiffness B_{sk} = 100 MPa, initial hydrate fraction S_{h0} = 80%, initial gas fraction S_{g0} = 0%, initial fluid pressure at the beginning of dissociation P = 5.5 MPa for pore size d = 10 nm and P = 3.0 MPa for pore size d = 30 nm. Note: The phase boundary *PB* shown corresponds to pure methane hydrate in unconfined sediments in Table 1: P [kPa] = exp (40.234 – 8860/T [K]); this expression is modified from *Sloan* [1998] using data computed with *HWHYD software* [2001].

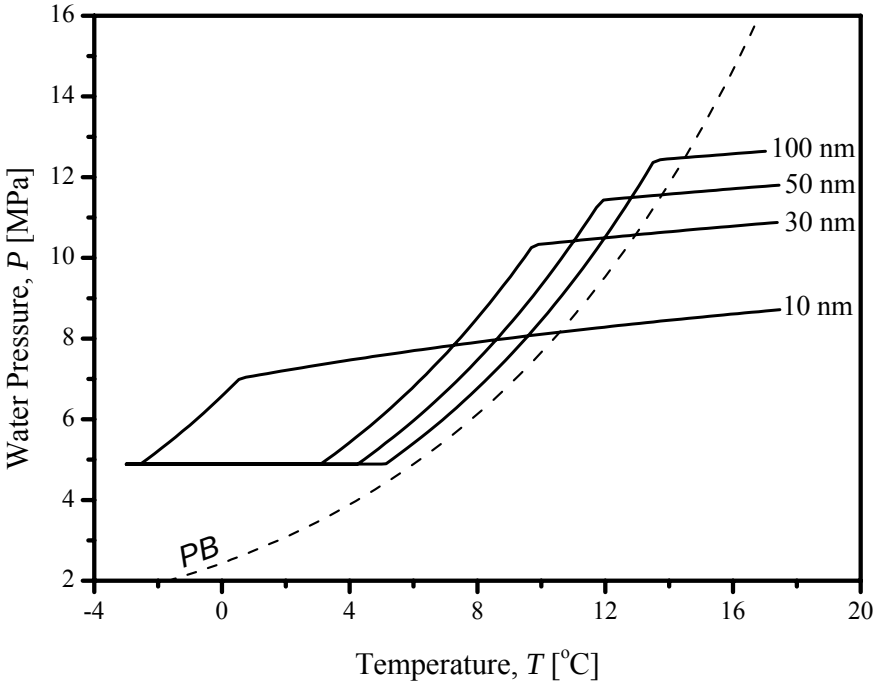

(a)

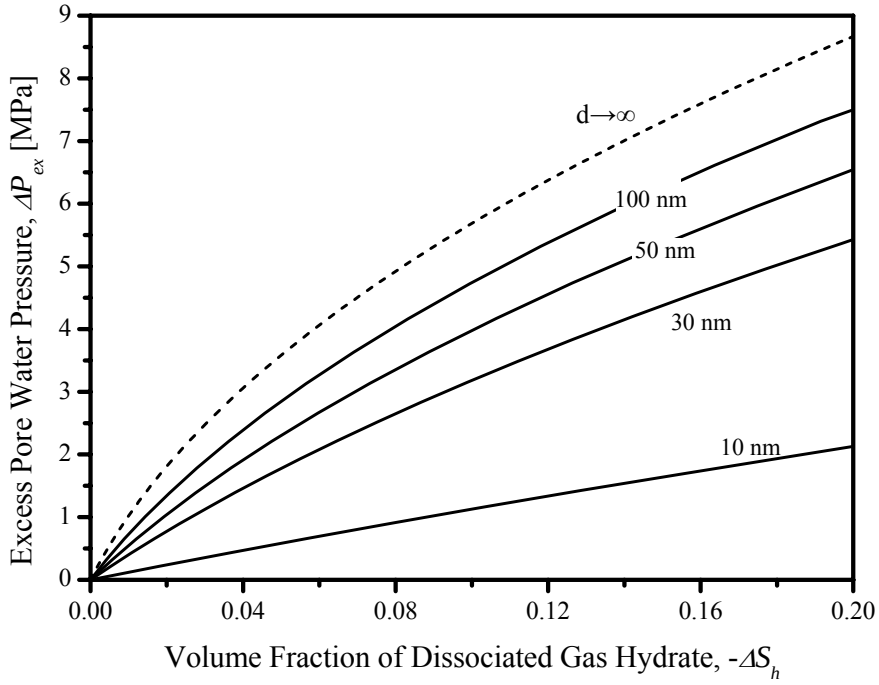

(b)

Figure 8. Effect of pore size on pore pressure generation. Initial conditions: sediment stiffness B_{sk} = 100 MPa, initial hydrate fraction S_{h0} = 20%, initial gas fraction S_{g0} = 0%, initial temperature T = -3C, and the initial fluid pressure P = 4.9 MPa. (a) Pressure-temperature trace in PT plane. (b) Pressure evolution during dissociation. Note: The phase boundary *PB* shown corresponds to pure methane hydrate in unconfined sediments in Table 1: P [kPa] = exp (40.234 – 8860/T [K]); this expression is modified from *Sloan* [1998] using data computed with *HWHYD software* [2001].